

Vertical transport of surface fire emissions observed from space

Siegfried Gonzi¹ and Paul I. Palmer¹

Received 8 June 2009; accepted 14 September 2009; published 27 January 2010.

[1] We use optimal estimation to infer the vertical distribution of surface emissions lofted from boreal and tropical biomass burning during June–October (JJASO) 2006. We use satellite observations of CO, a tracer of incomplete combustion, at thermal infrared and microwave wavelengths from Aura Tropospheric Emission Spectrometer (TES) and Microwave Limb Sounder (MLS), respectively. TES and MLS together typically provide two to three pieces of information. We use a maximum a posteriori (MAP) methodology to estimate emitted CO mass in five vertical regions spanning the troposphere and lower stratosphere, equivalent to estimating surface emissions. Correlations between neighboring vertical regions, due to vigorous mixing induced by surface heating, reduce the inversion to the information content provided by the data. We use a total of 1785 TES profile measurements, of which 672 are colocated with MLS. We define an injection height based on MAP statistics. We find that 10%–20% of boreal and tropical fire emissions, depending on the region, reach the free and upper troposphere during JJASO 2006. Our injection height estimates during two key pyroconvective events, Siberia (July) and Indonesia (October), qualitatively agree with measurements of aerosol index and attenuated backscatter from Aura Ozone Monitoring Instrument (OMI) and CALIPSO, respectively. Surface emissions inferred from our mass estimates agree with the Global Fire Emission Database biomass burning emission inventory to within $\pm 10\%$. The small percentage of emissions injected above the boundary layer result in disproportionate changes in CO concentrations of more than 2–25 ppb and 15–160 ppb over boreal and tropical regions, respectively.

Citation: Gonzi, S., and P. I. Palmer (2010), Vertical transport of surface fire emissions observed from space, *J. Geophys. Res.*, 115, D02306, doi:10.1029/2009JD012053.

1. Introduction

[2] Most heat released from free-burning fires is transferred into buoyant convective flows. The vertical extent of this mixing, much faster than boundary layer mixing, is a complex function of the fuel type, duration of burning, and the resulting meteorological conditions [Andrae *et al.*, 2004; Luderer *et al.*, 2006; Trentmann *et al.*, 2006; Rosenfeld *et al.*, 2007]. It is generally thought that burning emissions remain in the boundary layer (BL), occasionally reaching the free troposphere (FT) [Freitas *et al.*, 2006].

[3] However, there is mounting evidence from aircraft and satellite measurements [Fromm *et al.*, 2008; Damoah *et al.*, 2006; Jost *et al.*, 2004; Livesey *et al.*, 2004; Coheur *et al.*, 2007; Colarco *et al.*, 2004; Cook *et al.*, 2007] that intense surface heating associated with forest fires generates rapid vertical mixing, pyroconvection, which lofts copious amounts of trace gases and particles throughout the troposphere and lower stratosphere (LS). This rapid vertical

transport of trace gases and particles has implications for the atmospheric chemistry and transport of biomass burning pollutants, but the frequency of these extreme events remains unclear.

[4] Pyroconvection generally occurs on spatial scales much smaller than currently available with state-of-the-art global transport models and measurements from space, limiting our abilities to study its widespread impact on distributions of trace gases. State-of-the-art chemistry transport models that include biomass burning typically inject trace gases into the BL or heuristically inject mass throughout the troposphere based on sparse aircraft profiles [Leung *et al.*, 2007; Turquety *et al.*, 2007; Generoso *et al.*, 2007].

[5] We use carbon monoxide (CO), a general product of incomplete combustion, as a tracer of biomass burning. The main sink of CO is the hydroxyl radical (OH), with a resulting atmospheric lifetime of several weeks to a few months, long enough so that emitted plumes can be observed above background concentrations and short enough so that fresh emissions can be readily identified. We analyze colocated tropospheric nadir vertical profiles and upper troposphere/lower stratosphere (UT/LS) atmospheric limb measurements of CO from the NASA Tropospheric Emission

¹School of GeoSciences, University of Edinburgh, Edinburgh, UK.

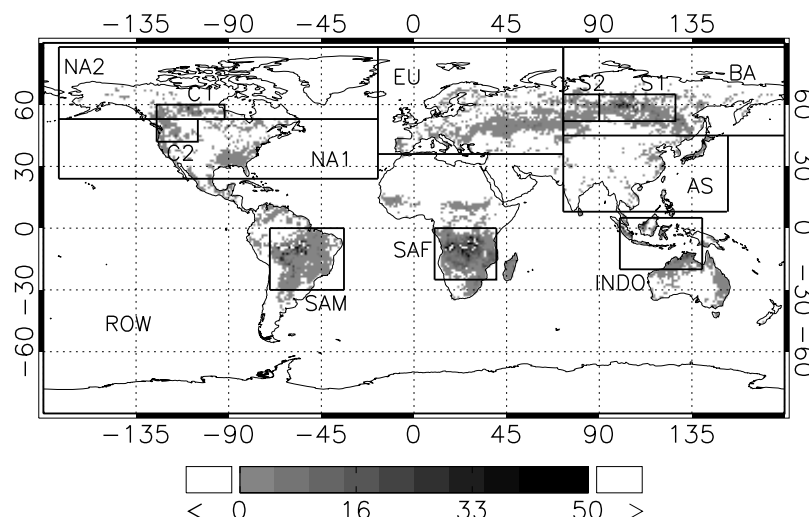


Figure 1. Emissions of CO from active fires during JJASO 2006 ($\text{g CO/m}^2/\text{JJASO}$) based on GFED (version 2) 8 day data. The following regions are used to determine initial conditions on 1 June 2006 for the inversion: North America (NA1 and NA2), Europe (EU), boreal Asia (BA), Asia (AS), Indonesia (INDO), South America (SAM), southern Africa (SAF), and rest of world (ROW). The following regions are used to study pyroconvection: Canada (C1 and C2), Siberia (S1 and S2), SAM, SAF, and INDO.

Spectrometer (TES) [Beer, 2006] and Microwave Limb Sounder (MLS) [Waters *et al.*, 1999], respectively, aboard the EOS-Aura satellite. The Aura satellite, described in section 2, has a local equatorial crossing time of 13:45, in ascending node, close to the expected diurnal peak of burning activity [Giglio, 2007]. The thermal infrared wavelengths used by TES have sensitivity to the lower troposphere (LT) when there is a significant thermal contrast between the LT and FT, as expected during intense surface heating from biomass burning. Over actively burning regions, TES and MLS observations typically provide a total of 2–3 pieces of information about CO in the troposphere. The GEOS-Chem chemistry transport model [Leung *et al.*, 2007; Turquety *et al.*, 2007] used here as the forward model to relate surface CO emissions to global 3-D CO concentrations (section 3), is sampled at the time and location of TES and MLS measurements and convolved with scene-specific instrument averaging kernels.

[6] The main focus of the paper is to estimate the vertical transport of biomass burning emissions during June–October (JJASO) 2006. To minimize model error due to nonburning sources of CO during JJASO we use a maximum a posteriori (MAP) (section 4.1) optimal estimation method to determine initial CO concentrations, by fitting model continental CO emissions (Figure 1) to TES CO observations during March–May 2006. To quantify the vertical transport of surface fire emissions we develop the MAP approach in section 4.2 to estimate the mass of emitted CO as a function of altitude, which is equivalent to the traditional surface flux inverse problem [Pfister *et al.*, 2005]. In section 5, we present the mean statistics, evaluate our injection heights for selected cases against cloud and aerosol layer heights inferred from Aura Ozone Monitoring Instrument (OMI) and CALIPSO, compare resulting emission estimates with Global Fire Emission Database (GFED),

and quantify the sensitivity of atmospheric CO concentrations due to prescribed injection heights. We conclude the paper in section 6.

2. TES and MLS CO Measurements

[7] The Tropospheric Emission Spectrometer (TES) and the Microwave Limb Sounder (MLS), two sensors aboard the NASA EOS-Aura satellite, were launched in July 2004 in a Sun-synchronous orbit. Both instruments measure atmospheric CO. TES is an infrared Fourier transform spectrometer that measures thermal emission in the 3–15 μm spectral region [Beer, 2006]. The ground footprint of each nadir observation is 5 km across track by 8 km along track. The along-track distance between successive nadir observations is approximately 182 km, achieving about 3400 individual soundings during global survey mode (26 h). We use vertical profile measurements of CO determined by optimal estimation [Bowman *et al.*, 2006] from data version Level 2 Global Survey Standard Products, V003, F04_04. TES CO profile concentrations, averaging kernels and error covariances are given for 67 pressure levels located mainly in the troposphere and stratosphere.

[8] TES CO profile observations typically have 1 to 2 bits of information in the troposphere, which degrade with increasing latitude [Rinsland *et al.*, 2006]. The information content reflects strong correlations between CO mixing ratios at individual pressure levels with each retrieved CO concentration a product of the contribution from all the other levels.

[9] Measurements of CO from the Microwave Limb Sounder (MLS) are used in conjunction with TES CO measurements to provide additional constraints in the UT/LS. MLS is a small radio telescope that scans the atmospheric

radiation along the atmospheric limb [Waters *et al.*, 1999]. CO is fitted using optimal estimation of measurements in two bands of the MLS 240 GHz radiometer, with a horizontal resolution of 400 km.

[10] We use version 2 MLS data and correct for a well characterized bias at two levels: dividing the 215 hPa MLS observation by a factor of 2 and reducing the 145 hPa MLS by 30% [Livesey *et al.*, 2008; Pumphrey *et al.*, 2007].

[11] MLS takes a limb measurement of an air mass, which is then observed 15 minutes later in the nadir by TES. We colocate cloud-free TES and MLS measurements using a two step approach: first, we identify measurements that fall into the same GEOS-Chem $2^\circ \times 2.5^\circ$ model grid (section 3), and second, we only consider TES and MLS measurements that are taken within 15 minutes of each other. We follow data quality screening protocols from the TES and MLS science team [Osterman *et al.*, 2007; Livesey *et al.*, 2007]. We focus on maximizing the spatial and temporal coverage from TES measurements that provide information about the lower and free troposphere, recognizing that vertical transport to the UT/LS due to surface burning is relatively infrequent.

3. Forward Model

[12] The forward model \mathbf{F} generally describes the relationship between the state vector \mathbf{x} and the measurement vector \mathbf{y} :

$$\mathbf{y} = \mathbf{F}(\mathbf{x}, b) + \epsilon, \quad (1)$$

where b represents model parameters that are not retrieved, e.g., in our problem nonbiomass burning sources of CO, and ϵ denotes the model error (e.g., chemistry, meteorology).

[13] In our work we use the forward model to describe the relationship between the state vector \mathbf{x} described by surface emissions of CO and atmospheric measurements of CO as observed by the TES and MLS instruments, \mathbf{y} . This is a three-step process.

[14] First, the GEOS-Chem global 3-D chemistry transport model relates surface emissions of CO to global 3-D distributions of CO concentration [Fiore *et al.*, 2003]. We use GEOS-Chem v7-04-10, driven by meteorological observations from the Goddard Earth Observing System v4 from the Global Modeling and Assimilation Office Global Circulation model based at NASA Goddard. We use this model at a horizontal resolution of $2^\circ \times 2.5^\circ$, with 30 sigma levels that span the surface to 0.01 hPa, 12 of which are below 10 km. The 3-D meteorological data is updated every 6 h, and boundary layer and tropopause heights are updated every 3 h.

[15] Primary sources of CO include biomass burning, fossil and biofuel combustion. Secondary sources are from the oxidation of coemitted volatile organic compounds (VOCs).

[16] We use 8 day mean biomass burning emission estimates from the Global Fire Emission Database (GFED version 2) [van der Werf *et al.*, 2006]. Fossil fuel distributions are based on 1985 values that have been scaled to 2006 values using liquid CO₂ usage [Palmer *et al.*, 2003]. The magnitude and distribution of fossil fuel emissions over eastern Asia are taken from more recent work [Streets *et al.*,

2006]. We use climatological biofuel emission estimates [Yevich and Logan, 2003]. We account for the secondary source of CO from the oxidation of VOCs by using empirical scaling factors based on oxidation yields determined by laboratory studies [Duncan *et al.*, 2007a].

[17] The main sink of CO is by oxidation with OH, resulting in an atmospheric lifetime of several weeks to a few months. We use precomputed monthly mean OH fields from a full-chemistry simulation for 2006, enabling us to linearly decompose CO contributions originating from individual sources and geographical regions. Although adjustment of CO sources should affect OH, the effect is inconsequential for estimating rapid vertical transport of CO using TES and MLS observations, which are directly overhead of the emissions. Using fixed monthly mean OH concentrations greatly simplifies calculation of the Jacobian matrix \mathbf{K} , used in the inversion calculations (section 4). We use a yearlong spin-up period (March 2005 to March 2006) to ensure that initial conditions are not present during the 2006 study period.

[18] Second, we sample the 3-D field of CO concentrations at the time and the location of each TES and MLS measurement in 2006. We discard model scenes with associated cloud optical depths greater than 1.0, which correspond to a 30% reduction in measurement sensitivity [Osterman *et al.*, 2007].

[19] Finally, we apply scene-dependent averaging instrument kernels, \mathbf{A} , which account for the vertical sensitivity of TES and MLS, to map from the 1-D CO concentration profiles, determined by GEOS-Chem, to TES and MLS measurement space (equation (3)). This final step is described in more detail below.

4. Inverse Model

[20] In this section, we describe two inverse model calculations using a maximum a posteriori (MAP) optimal estimation approach: (1) estimation of CO sources prior to JJASO 2006 and (2) estimation of the emitted mass of CO from burning as a function of altitude. As we discuss below, these two calculations are mathematically equivalent.

[21] Here, we outline the general methodology that is shared by the two calculations. Below we expand on calculation-dependent details. We use the MAP methodology:

$$\begin{aligned} \mathbf{x}_{i+1} &= \mathbf{x}_i + \left(\mathbf{K}_i^T \mathbf{S}_y^{-1} \mathbf{K}_i + \mathbf{S}_a^{-1} \right)^{-1} \\ &\quad \cdot \left[\mathbf{K}_i^T \mathbf{S}_y^{-1} (\mathbf{y} - \mathbf{F}(\mathbf{x}_i)) - \mathbf{S}_a^{-1} (\mathbf{x}_i - \mathbf{x}_a) \right] \\ \hat{\mathbf{S}} &= \left(\hat{\mathbf{K}}^T \mathbf{S}_y^{-1} \hat{\mathbf{K}} + \mathbf{S}_a^{-1} \right), \end{aligned} \quad (2)$$

where \mathbf{x} is the state vector, \mathbf{x}_a is the a priori state vector with associated errors described by the a priori error covariance matrix, \mathbf{S}_a . \mathbf{y} is the measurement vector with associated errors described by the measurement error covariance matrix, \mathbf{S}_y . \mathbf{K}_i is the Jacobian matrix, describing the sensitivity of \mathbf{y} to changes in \mathbf{x}_i . $\hat{\mathbf{S}}$ is the a posteriori error covariance matrix; $\hat{\mathbf{K}}$ is the a posteriori Jacobian matrix. The superscripts -1 and T denote matrix inverse and transpose operations, respectively.

Table 1. A Priori and a Posteriori CO Emissions and Their Respective Uncertainties Using TES Data Over March–May 2006 to Determine Background Concentrations on 1 July 2006^a

	NA	EU	AS	BA	ROW	INDO	SAM	SAF	CHEM
				<i>Fuel</i>					
A priori (Tg CO/MAM)	34.8	46.1	69.6	2.8	33.7				
A posteriori (Tg CO/MAM)	26.7	22.1	97.2	2.1	67.2				
\hat{S}_a	17.4	23.0	35.8	0.14	16.8				
\hat{S}	0.9	0.88	1.2	0.14	1.23				
post/prior	0.7	0.6	1.3	0.9	1.8				
$A_{ii}^{\#}$	1.0	1.0	1.0	0.02	1.0				
				<i>BB</i>					
A priori (Tg CO/MAM)	1.4	4.7	14.2	9.8	12.7	5.8	1.1	3.4	296.6
A posteriori (Tg CO/MAM)	1.1	12.2	40.8	7.0	25.2	−1.8	−1.1	7.7	257.0
\hat{S}_a	0.07	2.4	7.1	4.9	6.3	2.9	0.06	1.7	74.1
\hat{S}	0.07	0.9	0.7	0.7	0.3	0.2	0.05	0.3	1.5
post/prior	0.85	2.4	3.1	0.7	2.0	−0.29	−0.4	1.9	0.88
$A_{ii}^{\#}$	0.0035	0.86	1.0	0.98	1.0	1.0	0.17	0.96	1.0

^a \hat{S}_a , a priori uncertainty; \hat{S} , a posteriori uncertainty; MAM, March–May. Estimated fuel (sum of fossil fuel and biofuel) and biomass (BB) emissions (Figure 1) are from North America (NA = NA1 + NA2), Europe (EU), Asia (AS), boreal Asia (BA), Indonesia (INDO), South America (SAM), and southern Africa (SAF). We also estimate emissions from the rest of the world (ROW) and the secondary source of CO from VOC oxidation (CHEM). We use a posteriori values only where the retrieved inverse model averaging kernel $A_{ii}^{\#} > 0.5$, indicating that the estimate is well resolved by the TES data.

The subscript i denotes the i th iteration. All other variables are as previously defined.

4.1. Estimating Nonburning CO Sources Prior to JJASO 2006

[22] To minimize the bias between model and measurements during the 2006 JJASO burning season due to fossil and biofuel CO sources, we use the MAP approach (equation (1)) to determine CO concentrations on 1 June 2006 (initial conditions) using TES CO measurements between March and May (MAM) 2006.

[23] For this calculation, with reference to equation (1), the state vector \mathbf{x} includes CO emissions from fuel combustion (the sum of fossil fuel and biofuel) and biomass burning originating from North America (NA), Europe (EU), Asia (AS), boreal Asia (BA), southern Africa (SAF), South America (SAM), Indonesia (INDO), and rest of the world (ROW) as shown in Figure 1. The sum of fossil fuel and biofuel combustion accounts for the significant overlap of emission distributions [Palmer *et al.*, 2003]. For \hat{S}_a we assume a uniform uncertainty of 50% for continental emissions, and 25% for the secondary source of CO from CH₄ and NMVOC oxidation [Palmer *et al.*, 2003; Jones *et al.*, 2003].

[24] The measurement vector \mathbf{y} includes only CO measurements from TES during MAM, 2006. TES measurements are described as the natural logarithm of the CO concentration [Bowman *et al.*, 2006]. For this calculation, the forward model, including the GEOS-Chem CTM, $\mathbf{H}(\mathbf{x})$, relates surface emissions to TES measurements of CO, which are subsequently sampled at the time and location of TES measurements.

[25] We then use an interpolation matrix to map the model data to the 67 TES retrieved pressure levels (section 2). We also use the 67 levels to smooth the observation error covariance (equation (4)). Finally, we convolve the resulting profile with a scene-dependent instrument averaging kernel \mathbf{A} , which describes the vertical sensitivity of the instrument

to changes in atmospheric CO concentration. The forward model $\mathbf{F}(\mathbf{x})$ is described succinctly as

$$\mathbf{F}(\mathbf{x}) = \mathbf{y}_a + \mathbf{A}(\ln[\mathbf{H}(\mathbf{x}, b)] - \mathbf{y}_a), \quad (3)$$

where \mathbf{y}_a is the a priori CO concentration profile used for each profile retrieval.

[26] For each TES observation the observation error covariance, \mathbf{S}_y , in log space is created as follows:

$$\mathbf{S}_y = \mathbf{A}\mathbf{S}_M\mathbf{A}^T + \mathbf{S}_{noise}, \quad (4)$$

where \mathbf{S}_{noise} represents an estimate of instrument noise error, which we obtain with each TES observation, and \mathbf{S}_M represents the sum of forward model and representation error which we assume to be diagonal with a magnitude 40% of the CO concentration [Jones *et al.*, 2003]. Applying averaging kernels to \mathbf{S}_M ensures that the model error is smoothed in a consistent way to the instrument and that we account for the off-diagonal elements and cross correlations in the observation error covariance.

[27] Assuming fixed monthly mean OH concentrations (section 3) allows us to linearly decompose total CO into contributions from individual sources and regions. This greatly simplifies the calculation of the Jacobian matrix \mathbf{K} , describing the sensitivity of \mathbf{y} to changes in \mathbf{x} :

$$\mathbf{K}_i = \mathbf{A} \left[\frac{1}{\mathbf{H}(\mathbf{x}_i)_{trac}} \left(\frac{\partial \mathbf{H}(\mathbf{x}_i)_{trac}}{\partial \mathbf{x}} \right) \right], \quad (5)$$

where $\mathbf{H}(\mathbf{x}_i)_{trac}$ is a linearly decomposed tracer from a particular region and source.

[28] For the inverse model we use the tropospheric levels for TES. Using submatrices for \mathbf{K} , \mathbf{S}_y , \mathbf{y} , and $\mathbf{F}(\mathbf{x})$ reduces noise in the inversion and consequently increases the stability of the inversion.

[29] The inverse model averaging kernel, \mathbf{A}^* , is the analogue of the instrument averaging kernel, \mathbf{A} , and describes the ability of the measurements to infer the state vector, which in this calculation is surface fluxes of CO. A state vector element with a value of \mathbf{A}^* close to unity means that it is well constrained by the measurements.

[30] Table 1 shows that TES effectively constrains fuel emission estimates during MAM 2006 with the exception of BA where these emissions are small. A posteriori fuel emission estimates for NA and EU are 25% and 50% smaller than prior estimates, respectively. A posteriori fuel emission estimates for AS and ROW increase by 40% and 100%, respectively.

[31] TES also constrains biomass burning emission estimates over regions where the burning season is underway during MAM 2006, e.g., SAF, AS and BA. For this time period, we find that EU and AS prior biomass burning emissions underestimate the measurements by a factor of 2 and 3, respectively. Prior biomass burning emissions over BA overestimated the measurements by 30%.

[32] A posteriori SAM and INDO biomass burning emission estimates during MAM 2006, when fire activity is minimal, are slightly negative. SAM emissions are not well resolved by TES ($\mathbf{A}^* = 0.17$). INDO emissions, according to the averaging kernel, are well resolved by TES but may reflect large model errors in vertical transport of burning emissions, as discussed below. These results are largely insensitive to changes in a priori and measurement error, so we consider these estimates to be robust. We reemphasize that the importance of this calculation is to correct the nonburning emission sources of CO before we embark on a more detailed inverse model treatment of biomass burning emissions. We adjust the linear tagged tracers, corresponding to 1 June 2006, by using the ratio between a posteriori and a priori emissions (Table 1).

4.2. Estimating Vertical CO Mass Distribution

[33] To determine recent vertical transport of biomass burning emissions during JJASO 2006, we use all available TES and MLS measurements of CO over that period. Due to limitations of the available data the method is unable to identify the responsible process(es), and consequently, we interpret our results as an ensemble average for a particular region. For example, individual injection heights will not necessarily reflect the rapid vertical transport due solely to burning, instead reflecting nearby vertical transport due to other convective processes.

[34] We determine vertical transport of biomass burning emissions by fitting CO mass in the troposphere as a function of altitude using CO concentration measurements \mathbf{y} , which is equivalent to the conventional surface flux estimation problem [Pfister *et al.*, 2005]:

$$\frac{\partial \mathbf{y}}{\partial e} = \sum_i \frac{\partial m_i}{\partial e} \frac{\partial \mathbf{y}}{\partial m_i}, \quad (6)$$

where the left hand side and right hand side represent the sensitivity of \mathbf{y} to changes in emission e . This is equivalent to the sensitivity of mass m at altitude level i to a change in e , convolved with the sensitivity of \mathbf{y} to a change in m at

altitude i . $\partial \mathbf{y} / \partial m_i$ is similar to the instrument averaging kernel because of the relationship between mass and concentration, and $\partial m_i / \partial e$ can be thought of as the pyroconvection injection mass distribution.

[35] By virtue of the problem we are addressing and the fact that the forward model (section 3) does not generally inject biomass burning plumes above the BL, we artificially inject biomass burning CO into the troposphere over Canada (C1 and C2), Siberia (S1 and S2), SAM, SAF, and INDO during JJASO 2006 (Figure 1). All source magnitudes and distributions are as previously described.

[36] For an a priori injection profile, we calculate the typical number of model grid boxes that fall within the mean BL and tropopause height, based on assimilated meteorology, over the boreal and tropical regions during JJASO 2006, and use this fixed grid information throughout the study period. We acknowledge that the tropopause height over the tropical regions will typically be much higher than the boreal regions, but using the fixed altitude grid permits an easier comparison between boreal and tropical regions. To ensure we do not include unnecessary a priori information into our retrieval, we inject 22.5% of the total mass uniformly over four tropospheric altitude z regions (BL*, $z < 2$ km; lower FT, $2 \text{ km} < z < 5$ km; upper FT, $5 \text{ km} < z < 8$ km; and the UT, $8 \text{ km} < z < 11$ km); here BL* refers to the lowest 2 km of the atmosphere and does not correspond to the 3 hourly meteorology used by the forward model. We inject the remaining 10% of the total mass in the UT/LS ($11 < z < 15$ km), recognizing that pyroconvection may occasionally reach through the tropopause. Within an individual vertical region we assume the mass is uniformly mixed. We find that our analysis is generally insensitive to our assumed a priori injection profile.

[37] The forward model uses the averaging kernel for all levels of TES (67 pressure levels) and MLS (37 pressure levels) to estimate the model profiles and for smoothing observation error covariances.

[38] To construct the Jacobian matrix, \mathbf{K} , for each measured profile we use the closest spatial and 3 h BL height and tropopause height.

[39] For this calculation, with reference to equation (1), the state vector \mathbf{x} includes a five-element state vector, \mathbf{x} : m_{BL} , m_{LFT} , m_{UFT} , m_{UT} , and $m_{UT/LS}$, corresponding to the mass of CO (kg CO/15 min/per GEOS-Chem grid box) in the BL, lower and upper FT (LFT and UFT), the UT, and the UT/LS, respectively. The altitude ranges for these nominal vertical regions are 0 to BL for BL, BL to 5 km for the LFT, 5–8 km for the UFT, 8–11 km for the UT, and 11–15 km for the UT/LS. The UT/LS region, as defined here by altitude, is exclusively in the UT for the tropics. We use a five-element state vector to improve the model fit to the measurements, acknowledging that naturally strong correlations are present in neighboring state vector elements due to vertical mass transport.

[40] We assume a uniform value of 100% for \mathbf{S}_M that describes the CO mass in each vertical region, reflecting uncertainties in fuel loading, combustion completeness, area burned, and subgrid-scale meteorology. We assume a uniform value of 100% for diagonal elements of \mathbf{S}_a .

[41] The measurement vector \mathbf{y} includes CO measurements from TES and MLS during JJASO, 2006, as described above. For the inverse model we use a subsample of the full instrument averaging kernel used in the forward model: the tropospheric levels for TES and the 215 hPa and 147 hPa retrieval levels for MLS. Using submatrices for \mathbf{K} , \mathbf{S}_y , \mathbf{y} , $\mathbf{F}(\mathbf{x}_i)$ reduces noise in the inversion and consequently increases the stability of the inversion. We use the full TES and MLS matrices to build the error covariances and CO model profiles.

[42] The TES observation error covariance \mathbf{S}_y is as stated in section 4.1. \mathbf{S}_y for MLS is formulated in a similar manner (equation (4)) but in linear space.

[43] We do not consider the smoothing error [Rodgers, 2000] because we do not have high-resolution CO profile observations for our regions and times of interest. We therefore consider the retrieval as an estimate of a smoothed version of the state vector, rather than an estimation of the complete state.

4.2.1. Convergence Criterion

[44] We use the following convergence criterion [Connor *et al.*, 2008]:

$$(\mathbf{x}_i - \mathbf{x}_{i+1})^T \hat{\mathbf{S}}^{-1} (\mathbf{x}_i - \mathbf{x}_{i+1}) < n, \quad (7)$$

where n is the number (=5) of state vector elements. We find 2%–3% of all our inversions fail this convergence criteria, which we discard. Convergence is generally reached within 2 or 3 iterations of the MAP approach.

4.2.2. Inversion Information Content

[45] We use the prewhitened Jacobian, $\tilde{\mathbf{K}}$, to determine the resolution of the state vector for each inversion:

$$\tilde{\mathbf{K}} = \mathbf{S}_y^{-1/2} \mathbf{K} \mathbf{S}_a^{1/2}. \quad (8)$$

The number of singular values of $\tilde{\mathbf{K}}$ greater than unity provides an indication of the number of pieces of information that can be retrieved from the inversion. We find that in nearly all our vertical mass retrievals the effective rank of the prewhitened Jacobian is typically 2 or 3, reaching 4 under some rare circumstances, supporting our use of a five-element state vector. The degrees of freedom (not shown here) in all our cases of the a posteriori state vector solution typically lies between 1.5 and 3.0.

4.2.3. Definition of Injection Height

[46] We define the injection height as the maximum height at which the a posteriori mass is higher than the a priori mass and the a posteriori uncertainty is 50% smaller than the a priori value. This is described using the following criterion:

$$\left(\frac{\hat{\mathbf{S}}_{ii}}{\mathbf{S}_{a_{ii}}} \right) \leq 0.5 \wedge (\mathbf{x}_{p_i} \geq \mathbf{x}_{a_i}) \vee (\mathbf{x}_{p_i} \geq \mathbf{x}_{p_1}), \quad (9)$$

where \mathbf{x}_p represents the a posteriori state vector; \vee and \wedge denote the mathematical terms “and” and “or,” respec-

tively, and all other variables are as previously defined. The subscript i is from 1 to 5. Our criterion is based on the assumption that once the a posteriori error is reduced by a factor of 2, i.e., $(\hat{\mathbf{S}}_{ii}/\mathbf{S}_{a_{ii}} < 0.5)$, the solution in the state vector is not significantly influenced by the a priori state vector assumption [Rodgers, 2000].

[47] For each retrieval, we start from the surface (BL, index $i = 1$) and move up to the UT/LS ($i = 5$), testing if the criterion in equation (9) is met at each level. The last index for which the criterion is met is the injection height. The strict criterion is met by 33% of the retrievals. As a conservative approach we interpret the remaining 67% of converged retrievals, which have a posteriori uncertainties that have been reduced by less than 50%, as having BL injection heights.

5. Results

[48] Here, we present the mean statistics of our retrieved injection height over JJASO 2006 for each study region shown in Figure 1.

[49] We compare the associated a posteriori biomass burning emissions with corresponding values from the GFED inventory [van der Werf *et al.*, 2006].

[50] To help evaluate our retrieved injection heights, particularly those associated with transport to the FT and UT, we present two cases: (1) Siberia, July 2006; and (2) Indonesia, October 2006. We use (1) aerosol index (AI) measurements from the Aura Ozone Monitoring Instrument (OMI), which track the transport of smoke aerosol from surface fires, and (2) measurements of backscatter attenuation from the NASA CALIPSO satellite [Vaughan *et al.*, 2004], which provide profiles of cloud and aerosol properties. Further information about OMI and CALIPSO (and how these data can provide information on aerosol size and hydration) can be found in Appendix A.

[51] We quantify the importance of our retrieved injection heights on determining tropospheric composition using the GEOS-Chem chemistry transport model.

5.1. Mean Statistics of Injection Heights

[52] During JJASO 2006 we find a total of 1785 TES CO profiles, of which 672 are colocated with MLS CO profiles.

[53] Figure 2 shows the mean statistics of injection heights during JJASO 2006. We find no significant regional variations in pyroconvection injection heights over Siberia and Canada, where 11%–19% of observed plumes reach the FT and UT. Analysis of plume height data derived using multiangle imaging and lidar measurements over Canada in 2006 showed that 5%–20% of all plumes are transported out of the BL [Mazzoni *et al.*, 2007; Kahn *et al.*, 2008]. Over SAF, where the fuel source is mainly savanna, we find that less than 10% of plumes are transported out of the BL. Over SAM, approximately 17% of the burning emissions are injected out of the BL, supporting findings based on airborne measurements that injection heights higher than the BL over the Amazon are not uncommon [Andreae *et al.*, 2001]. Over INDO, where deep convection is frequent during September and October [Duncan *et al.*, 2007b], we find that up to 23% of emissions were injected into the FT and UT, with 4% reaching higher than 11 km. Fire activity

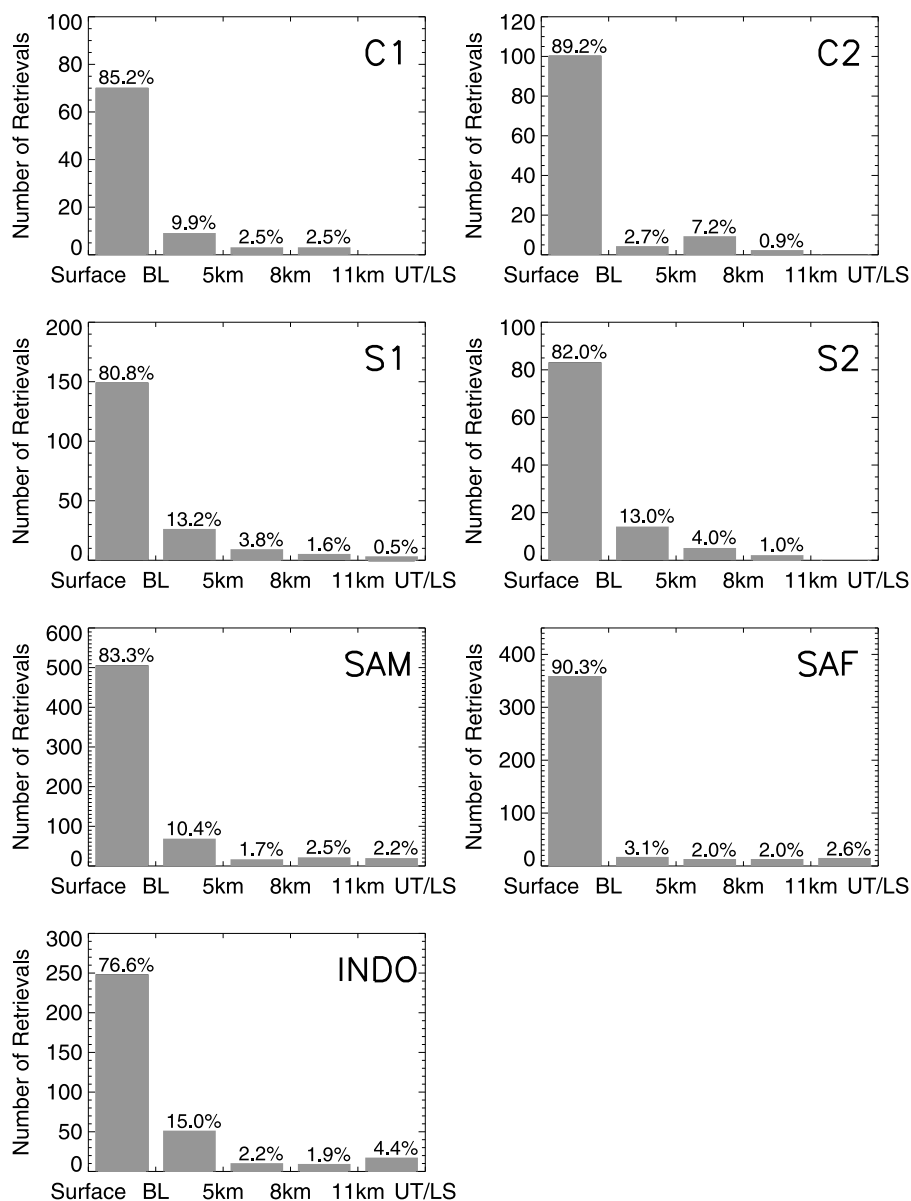


Figure 2. Absolute and percentage frequency distribution of retrieved BB injection heights for C1, C2, S1, S2, SAM, SAF, and INDO (Figure 1) during JJASO 2006 for five distinct crude atmospheric regions. These data represent retrievals using all TES CO data, as well as colocated MLS data, where available.

over this region was anomalously high during October 2006 due to El Niño [Logan *et al.*, 2008; Nassar *et al.*, 2009]. Observed values of CO from TES and MLS, and of formaldehyde, another tracer of biomass burning, from the OMI aboard Aura (T. Kurosu, Harvard-Smithsonian Center for Astrophysics, personal communication, 2009), over Indonesia during October 2006 are some of the highest in their record.

[54] The mean statistics using only TES CO profiles is similar to those shown here but with no injected mass in the UT/LS and consequently more injected mass in the free troposphere, reflecting the important role of MLS data in better estimating transport in the UT/LS.

5.2. Evaluation of A Posteriori CO Emissions

[55] As explained above, vertically integrating our retrieval of mass redistribution is equivalent to estimating surface emissions (equation (1)). Table 2 shows that our a posteriori emission estimates are typically within 10% (range from 2% to 23%) of a priori emissions provided by the Global Fire Emission Database [van der Werf *et al.*, 2006] over the regions studied.

[56] We find that for a large number of retrievals the vertical CO mass is redistributed, sometimes dramatically, while the total column CO mass is conserved within uncertainty (not shown). Table 2 shows that when we consider only the retrievals for which we can confidently determine an injection height, a posteriori emissions are

Table 2. A Priori and a Posteriori Hourly Biomass Burning Emission Estimates and Related Uncertainties Over the Model Regions as Sampled by the TES and MLS Satellite Instruments During JJASO 2006^a

Region	A Priori Emissions (mg CO/m ²) $\pm\sigma$	A Posteriori Emissions (mg CO/m ²) $\pm\sigma$	TES+MLS ^b
C1	110.1 \pm 15.9; 21.6 \pm 5.4	108.0 \pm 12.0; 17.7 \pm 3.9	81 (39); 27 (14)
C2	17.5 \pm 1.8; 7.3 \pm 0.9	16.5 \pm 1.4; 6.9 \pm 0.7	111 (49); 48 (18)
S1	407.8 \pm 33.0; 156.5 \pm 18.2	336.2 \pm 23.7; 119.9 \pm 12.6	182 (83); 62 (29)
S2	66.1 \pm 6.9; 36.0 \pm 6.0	56.7 \pm 5.0; 28.3 \pm 4.3	100 (50); 27 (14)
SAM	561.0 \pm 36.7; 266.0 \pm 26.8	598.5 \pm 26.5; 256.1 \pm 19.2	599 (204); 217 (70)
SAF	806.1 \pm 37.9; 363.1 \pm 25.3	871.2 \pm 28.3; 370.9 \pm 18.6	392 (140); 125 (48)
INDO	913.9 \pm 143.9; 274.3 \pm 53.4	1044.8 \pm 107.4; 288.3 \pm 41.2	320 (107); 94 (40)

^aRelated uncertainties, σ . Model regions are shown in Figure 1. Each region consists of two entries: (1) emissions inferred from using all converged inversions and (2) emissions inferred from using inversions only where an injection height could be determined (33% of all successful inversions). Figure 2 results from including all converged inversions.

^bThe corresponding numbers of TES plus MLS observations (the numbers in parentheses denote colocated MLS observations).

typically lower than a priori emissions over boreal regions and higher than a priori emissions over tropical regions; this situation is similar if we include all converged retrievals (Table 2).

5.3. Evaluation of Siberian Fires in July 2006

[57] Large forest fires occurred over Siberia during July 2006, which were associated with significant photochemical processing, resulting in elevated concentrations of tropospheric O₃ [Verma *et al.*, 2009].

[58] Figure 3 shows that over Siberia on 26 July, AI values at the core of the smoke plume are larger than 10, representing some of the highest values observed during a typical burning season and provide an indication that particles have been transported in the UT/LS [Fromm *et al.*, 2008]. Figure 4 shows CALIPSO attenuation measurements for that time and region, which suggest cloud top heights between 10 and 15 km, independently confirming the high AI measurements. The nearest TES/MLS measurements are 100 km away (not shown).

[59] As this smoke plume travels northeastward AI values decrease due to atmospheric dispersion, but are still above 10 on 28 July when TES and MLS overpass (Figure 3). Nearby CALIPSO attenuation backscatter measurements, available on 27 July, suggest that cloud top heights are between 10 and 15 km (Figure 4); a nearby CALIPSO overpass is not available on 28 July.

[60] On 28 July, Figure 5 shows that TES measurements of CO in the LT, where the instrument is sensitive to CO during surface burning, is in excess of 200 ppb; MLS CO observations, above 10 km, are close to 200 ppb, a reflection of rapid vertical transport. We find that 60% of the total column over this region is due to regional biomass burning (not shown), corresponding to an a posteriori mass increase

in the LFT and UT and a decrease in the UFT, with the total column mass increasing by only 5%. For this retrieval we find the injection height is above 10 km, consistent with the large observed AI.

[61] On 29 July, OMI AI is 8.5 corresponding to elevated CALIPSO attenuated measurements at 10 km (Figure 4). No TES and MLS measurements were close by.

[62] Only TES data is available on 30 July (Figure 3), after the plume has traveled further east (AI = 6.5). CALIPSO data suggests nearby cloud top heights of approximately 11 km (Figure 4). The retrieved a posteriori mass has increased by 3% and corresponds to an injection height between 5 and 8 km (Figure 5).

5.4. Evaluation of Indonesian Fires During October 2006

[63] Atmospheric concentrations of CO and O₃ over Indonesia and surrounding regions, observed by TES during October–December 2006, were higher than those observed in 2005 by 15–30 ppb and more than 80 ppb, respectively [Logan *et al.*, 2008]. This was due primarily to elevated biomass burning emissions, associated with anomalously low rainfall, resulting from moderate El Niño conditions.

[64] Figure 5 shows that over Indonesia on 22 October, TES observed CO concentrations greater than 400 ppb throughout the LT and greater than 500 ppb over 4–8 km while MLS observed more than 250 ppb above 10 km. For this fire, the a posteriori column mass increased by 50% and features a strong two-peak structure (characteristic of tropical cloud top height distributions [Dessler *et al.*, 2006]), with values of more than 600 ppb over 1–3 km and more than 400 ppb over 8–10 km, resulting in an injection height greater than 11 km. Considering the broad averaging kernels associated with TES and MLS (e.g., Figure 5) we cannot localize the injection height beyond the crude vertical regions over which we estimate CO mass (section 4.2).

[65] Figure 6 shows that nearby CALIPSO observations infer cloud top heights of more than 13 km on this day, indicative of the vertical extent of transport, consistent with our estimate of injection height. Figure 7 shows a nearby radiosonde profile on 22 October. The radiosonde shows that the level of neutral buoyancy, the height at which a rising parcel of air reaches a temperature equilibrium with the surrounding air, is 138 hPa which is close to 14 km, again consistent with our retrieved injection height. CALIPSO also shows an extended aerosol layer at 4 km (indicated by an arrow in Figure 6) according to the official vertical feature mask data product (not shown), which may explain the low OMI AI of less than 4 over this region.

5.5. Sensitivity of CO Concentrations to Prescribed Injection Heights

[66] Here, we assess the importance of our results to quantitatively understanding atmospheric composition using the GEOS-Chem CTM (section 3). We use the seasonal average injection heights (JJASO 2006) for each study region (Figure 2) to vertically distribute surface emissions and compare the resulting 3-D distribution of CO concentrations (hereinafter, referred to as the perturbed calculation) with CO concentrations from a control calculation that adopts the common assumption of BL injection.

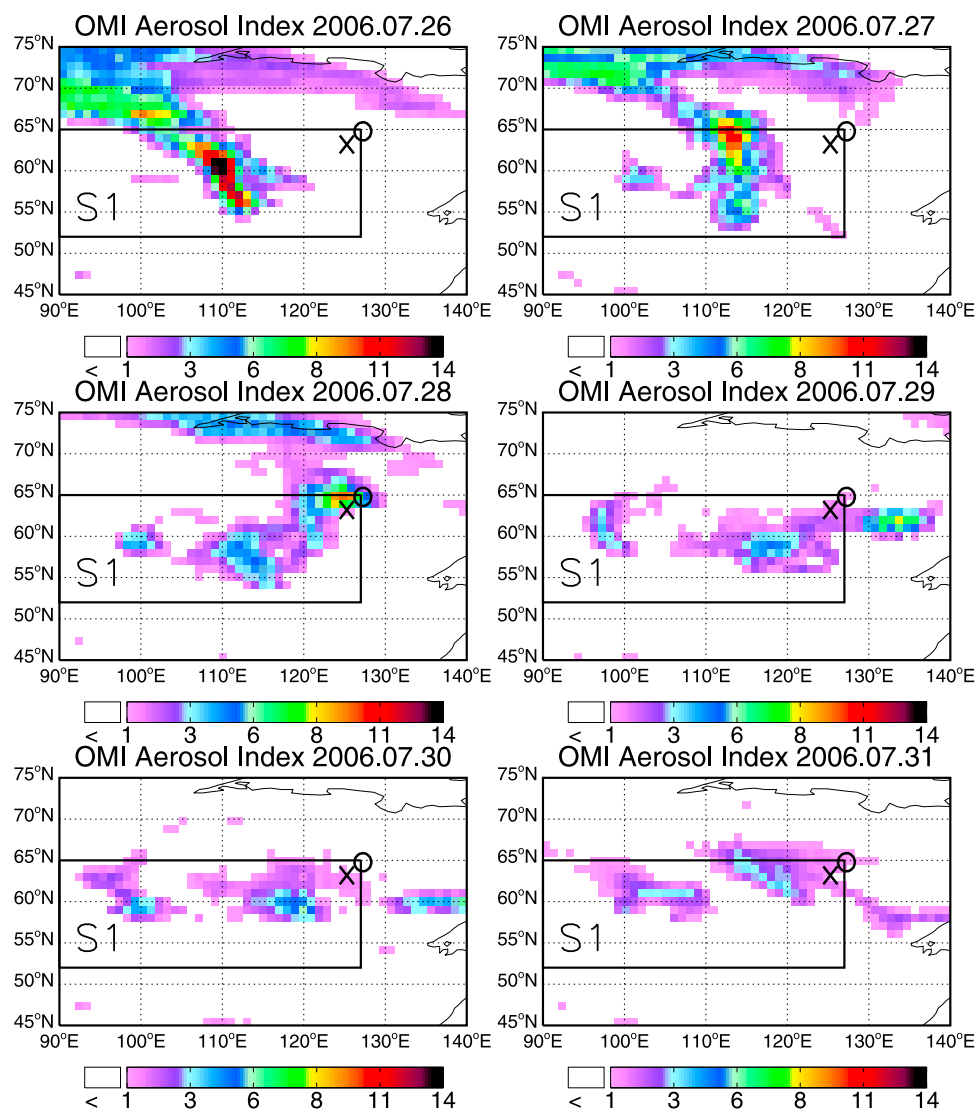


Figure 3. Distributions of aerosol index (unitless) observed by the Ozone Monitoring Instrument over Siberia (region S1; Figure 1) during 26–31 July 2006. The crosses and circles denote the locations of TES and MLS profile measurements on 28 July and of TES measurements on 30 July, respectively. The corresponding profile measurements of CO are shown in Figure 5. Corresponding CALIPSO lidar observations are shown in Figure 4.

[67] Figure 8 shows the meridional monthly means of perturbed minus control runs for the tropical (0°S – 30°S) and boreal (42°N – 67°N) study regions. In general, differences are characterized by a decrease of CO in the BL and an increase in CO in the FT and UT, with a seasonal variation determined by burning activity over these regions.

[68] Over the tropics, differences in CO concentrations over SAF range from a decrease of 10–25 ppb in the BL and an increase 5–10 ppb, with largest values occurring during June–August. Over SAM, the magnitude of differences are similar to those over SAF, but peak later in August and September. Indonesian burning appears in August but peaks in October, as reported in this paper, with BL reductions that range between 70 and 160 ppb and FT/UT increases ranging between 20 and 150 ppb.

[69] In contrast, using seasonal-averaged injection heights over Siberia and Canada result in much smaller CO concentration perturbations. Canadian fires peak in June with a reduction of up to 3 ppb in the BL and increase in the FT of up to 2 ppb. Siberia fires, peaking in July, lead to reductions of 2–26 ppb in the BL and to increases of 1–15 ppb in the FT.

6. Summary and Concluding Remarks

[70] We infer vertical transport of CO from biomass burning emissions during June–October (JJASO) 2006 using colocated thermal infrared and microwave measurements of CO from the Tropospheric Emission Spectrometer (TES) and the Microwave Limb Sounder (MLS), respectively, aboard the NASA Aura satellite.

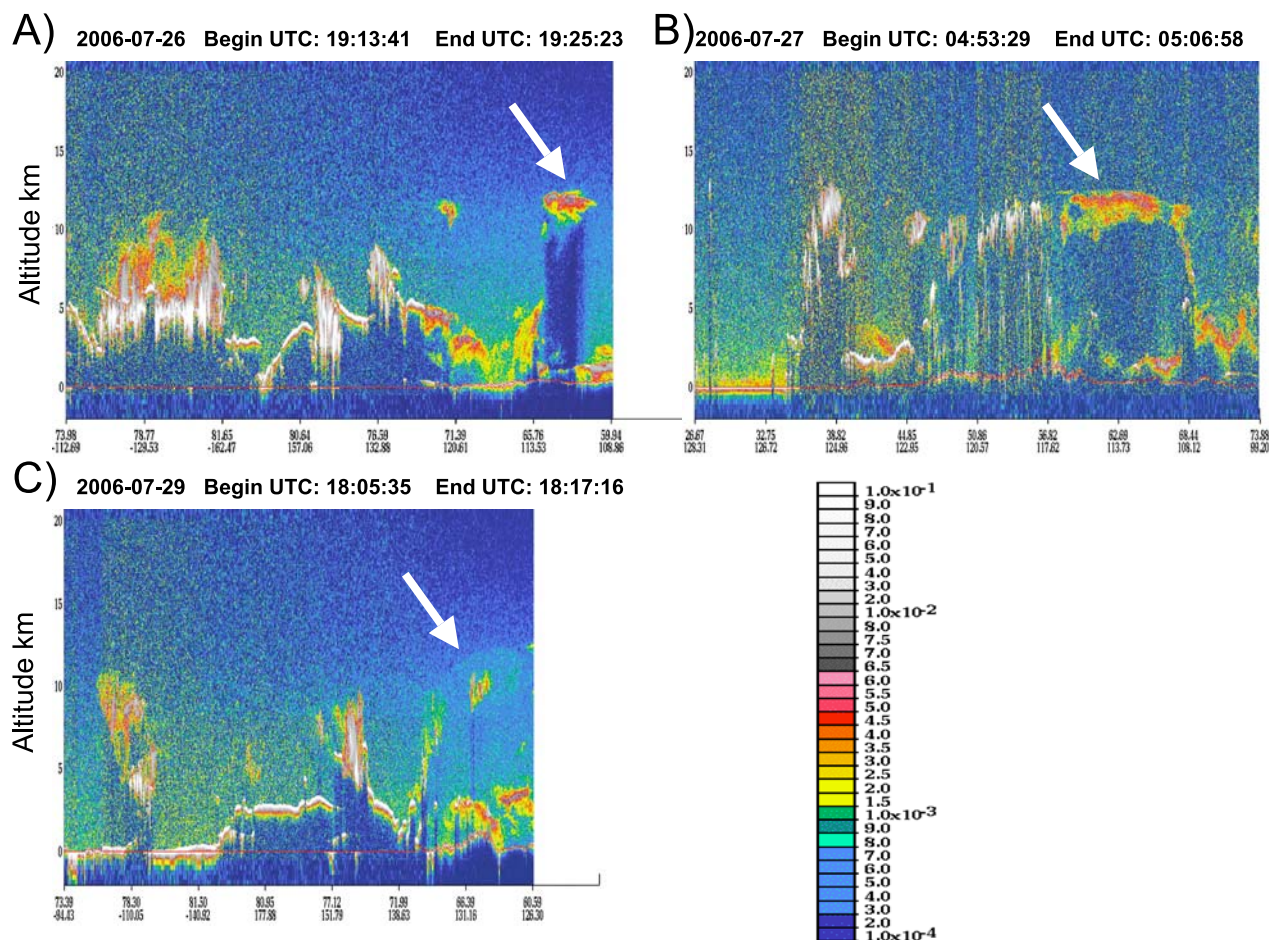


Figure 4. CALIPSO total attenuated backscatter measurements for the region S1 (Figure 1) during (a) 26, (b) 27, and (c) 29 July 2006. The x axis denotes the latitude and longitude along the satellite orbit, and the y axis denotes height (km). The time of observation can be found at the top of each plot. Figures 4a and 4b suggest cloud top heights at 10 km (indicated by white arrows) close to the smoke plume center observed by OMI (60°N , 110°E and 65°N , 113°E) on 26 and 27 July 2006, respectively (Figure 3). Figure 4c shows CALIPSO observations next to the smoke center plume with the highest AI for that day over the region S1 (Figure 3) (62°N , 133°E).

[71] The forward model relates the vertical transport of CO mass from biomass burning emissions to TES and MLS concentration measurements of CO.

[72] We develop a maximum a posteriori (MAP) inverse model approach to estimate recently emitted CO mass from biomass burning as a function of altitude. We estimate CO mass over five regions: boundary layer, lower free troposphere (BL to 5 km), upper free troposphere (5–8 km), upper troposphere (8–11 km), and upper troposphere/lower stratosphere (11–15 km). TES and MLS measurements typically include 2–3 pieces of information. We use the five regions to improve data fitting only, acknowledging that rigorous vertical mixing associated with surface fires introduce strong correlations between neighboring regions, consequently reducing the problem to the information content provided by the data. Because of the broad instrument averaging kernels of TES and MLS we cannot localize the injection height beyond the crude vertical regions over which we estimate CO mass.

[73] Due to limitations of the available data the method is unable to identify the responsible process(es), and consequently, we interpret our results as an ensemble average for a particular region.

[74] We do not find large regional variations of injection heights between the two boreal (Canada and Siberia) and three tropical (South America, southern Africa and Indonesia) regions. We typically find that only 10%–25% of emissions are injected above the boundary layer, with only a few percent reaching the upper troposphere; the largest percentage of high-altitude injections were over Indonesia during October. Our results over boreal latitudes are consistent with plume heights determined by multiangle imaging measurements [Mazzoni *et al.*, 2007; Kahn *et al.*, 2008]. We use our retrievals, averaged on a regional scale, to vertically distribute surface emissions to show that the small percent of emissions that get lofted out of the boundary layer have a disproportionate impact on atmospheric concentrations, with potential errors greater than 100 ppb over Indonesia.

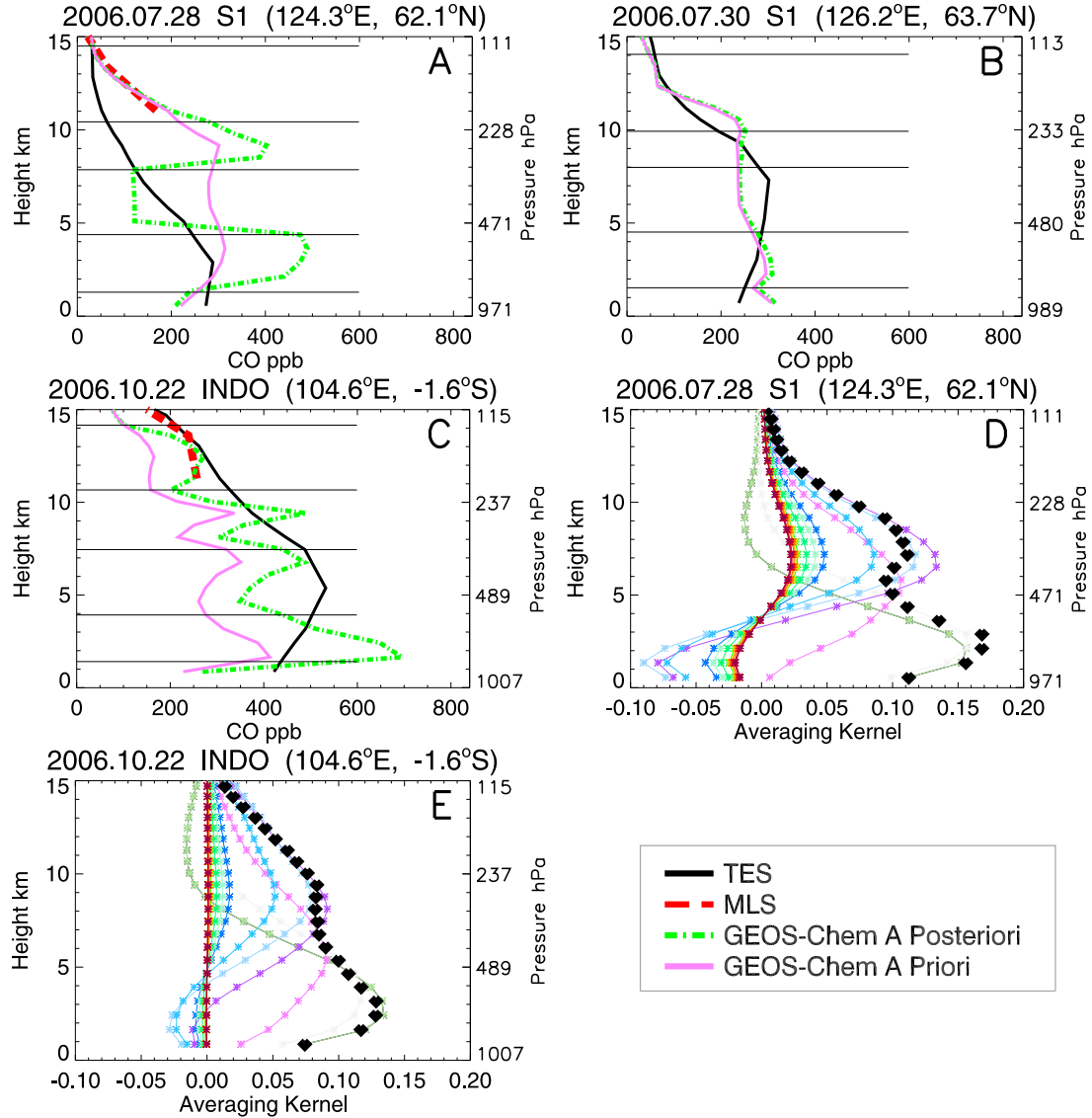


Figure 5. Observed a priori and a posteriori model vertical distributions of CO (ppb) over Siberia during (a) 28 and (b) 30 July 2006 and over Indonesia during (c) 22 October 2006. Retrieved mass distributions of CO are converted to ppb. The grey horizontal lines define the five fitted regions: BL, LFT, UFT, UT, and UT/LS. Solid black and dashed red lines denote TES and MLS CO concentrations, respectively. The pink dash-triple-dotted and green dash-dotted lines denote the a priori and a posteriori CO profile in model space, respectively. Averaging kernels from TES on individual retrieved pressure levels, denoted by different colors, are shown for scenes over (d) Siberia and (e) Indonesia. The large diamonds denote the trace of the averaging kernel matrix for every retrieval level.

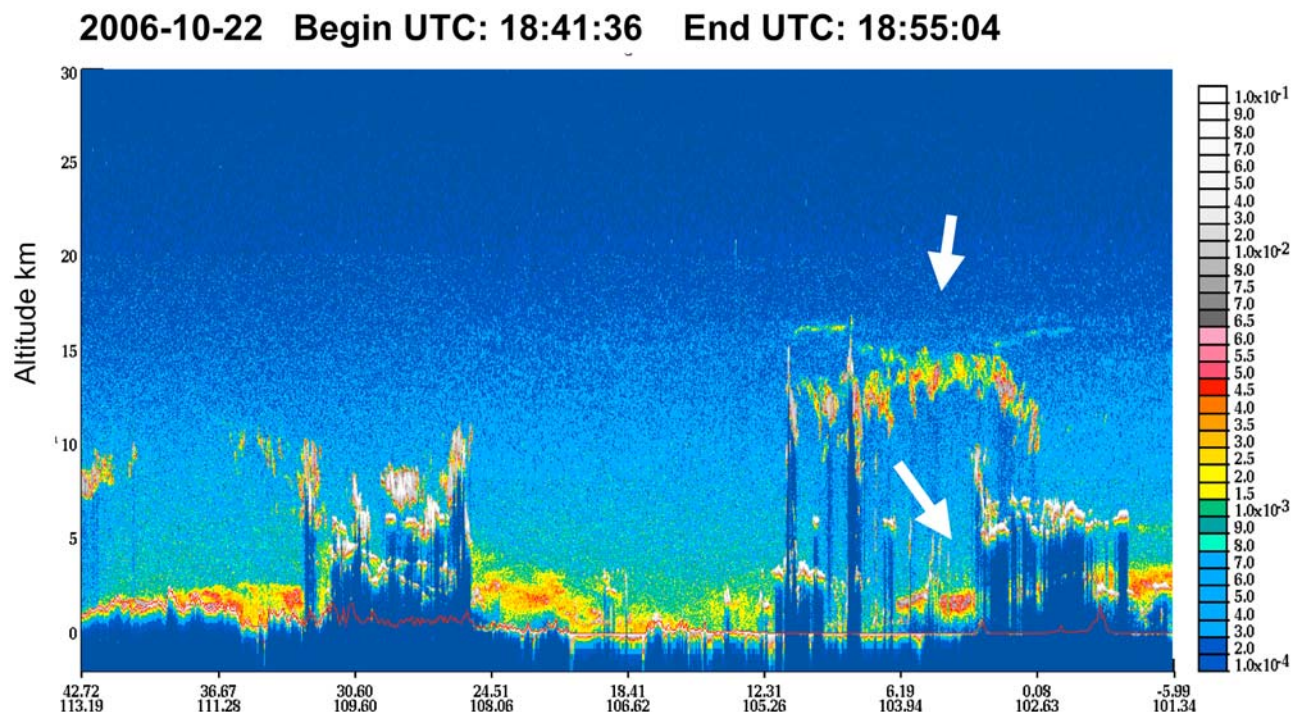


Figure 6. CALIPSO total attenuation backscatter measurements, as described by Figure 4 but over Indonesia (-1.6°S , 104.6°E) on 22 October 2006.

[75] We evaluate our retrievals using two approaches. First, we vertically integrate our retrievals of mass redistribution and compare them with our retrieval a priori emissions from the Global Fire Emission Database v2. Our a posteriori emission estimates are typically within 10% (range from 2% to 23%) of a priori emissions over the regions studied. We find that for a large number of retrievals the vertical CO mass is redistributed, sometimes dramatically, while the total column CO mass is conserved within uncertainty.

[76] Second, we evaluate our retrievals during two case studies of surface burning: one over large Siberian forest fires during July 2006, associated with significant photochemical processing [Verma *et al.*, 2009], and one over Indonesia during October 2006 associated with anomalously high fire activity due to El Niño [Logan *et al.*, 2008; Nassar *et al.*, 2009].

[77] In both cases, our retrieved injection heights are consistent with (1) aerosol index (AI) measurements from Aura Ozone Monitoring Instrument (OMI), which track the transport of smoke aerosol from surface fires, and (2) measurements of backscatter attenuation from the NASA CALIPSO satellite, which provide profiles of cloud and aerosol properties.

[78] We have shown that incorrect prescription of vertical transport of biomass burning emissions, particularly over the tropics, can lead to serious model error in the distribution of CO. This also has implications for the rapid vertical transport of shorter-lived trace gases emitted by fires, which would normally remain in the boundary layer, and the subsequent atmospheric chemistry [Prather and Jacob, 1997]. This model error, without proper characterization,

has far-reaching implications for inverse model calculations that use chemistry transport models to relate observed distributions of atmospheric trace gas concentrations to surface sources and sinks, particularly interpreting data over regions with strong vertical transport. This problem may be more acute with satellite observations that represent vertically weighted measurements of the atmospheric profile. Quantifying the associated errors in a posteriori biomass burning estimates will be the subject of future work.

[79] Our retrieved product provides limited vertical resolution of vertical transport of pollutants, but this is sufficient to provide crucial information about horizontal detrainment of the vertical transport of pollutants that can inform larger-scale models. We can only retrieve plume vertical transport over scenes free of clouds and aerosols. However, our MAP technique is sufficiently generic that it could be applied to other trace gases that include a large contribution from biomass, e.g., HCN or HCHO, provided the data are sensitive to different vertical regions through the troposphere. Even with the current trend of reducing model resolution it is unlikely that the community will be running a resolution necessary to accurately describe pyroconvection within 5–10 years, so until then large-scale models will have to rely on parameterizations constrained by available data. We therefore anticipate our work to be a starting point from which newer, higher-resolution space-borne sensors will be used to develop more comprehensive parameterizations of pyroconvection. We propose that integrating colocated information from land-surface properties (e.g., fire radiative power, FRP) and resulting emissions of trace gases could be the most fruitful approach, provided we

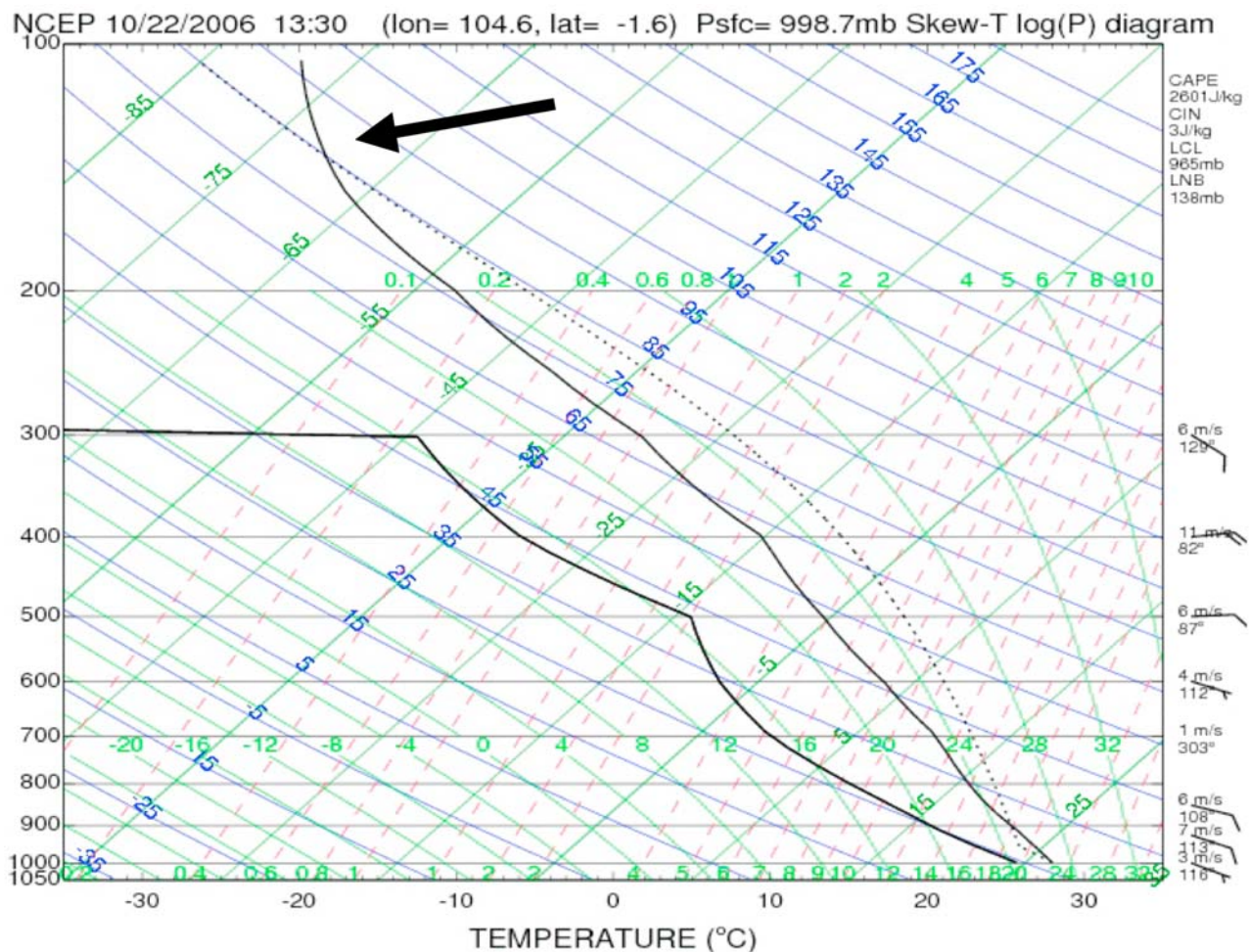


Figure 7. A log(pressure)-temperature diagram from an NCEP radiosonde (-1.6°S , 104.6°E) on 22 October 2006. The black arrow indicates the height in the atmosphere (138 hPa, ≈ 14 km) where the temperature (black solid line) crosses the moist adiabatic line (black dotted line) and marks the level of neutral buoyancy.

understand the relationship between FRP and the resulting energy allocated to convection.

Appendix A: OMI Aerosol Index Data and CALIPSO Total Attenuation Backscatter Measurements

[80] We use OMI aerosol index (AI) values and CALIPSO total attenuation backscatter observations to provide correlative information for our vertical transport of injection heights derived from TES and MLS CO measurements.

[81] The Ozone Monitoring Instrument (OMI), aboard the NASA Aura platform, measures solar-backscattered UV radiation in the range 270–500 nm with a ground footprint of $13 \times 25 \text{ km}^2$, achieving daily global coverage [Levelt *et al.*, 2006]. The AI quantity uses the ratio of observed backscattered radiation at 360 nm and a similar atmosphere that includes only Rayleigh scattering [Torres *et al.*, 1998]. The AI is sensitive to the height of the atmospheric aerosol layer, and therefore the magnitude can provide a crude indication of the height of this layer [Herman *et al.*, 1997; Zhang *et al.*, 2005].

[82] The joint NASA-CNES Cloud-Aerosol Lidar and Infrared Pathfinder Satellite Observations (CALIPSO) instrument was launched in April 2006 aboard the NASA Aqua platform, into the same Sun-synchronous orbit as the NASA Aura platform, with an equator-crossing time of 1:30 pm. CALIPSO uses a lidar with orthogonal polarization to measure vertical profiles of elastic backscatter at 532 and 1064 nm from the surface to 40 km that are used to retrieve cloud and aerosol properties during day and night [Winker *et al.*, 2006; Vaughan *et al.*, 2004].

[83] Broadly, the CALIPSO retrievals algorithms use the two wavelengths to provide information about aerosol size; and use the two orthogonal polarization components of the 532 nm wavelength to help differentiate between ice clouds, water clouds, and mixed phase clouds [Vaughan *et al.*, 2004].

[84] We use total attenuation backscatter measurements from CALIPSO, an official data product (see <http://www-calipso.larc.nasa.gov/products/>), to infer cloud and aerosol properties over Siberia and Indonesia. We have also analyzed the accompanying CALIPSO vertical feature masks to confirm the cloud and aerosol morphology as indicated by

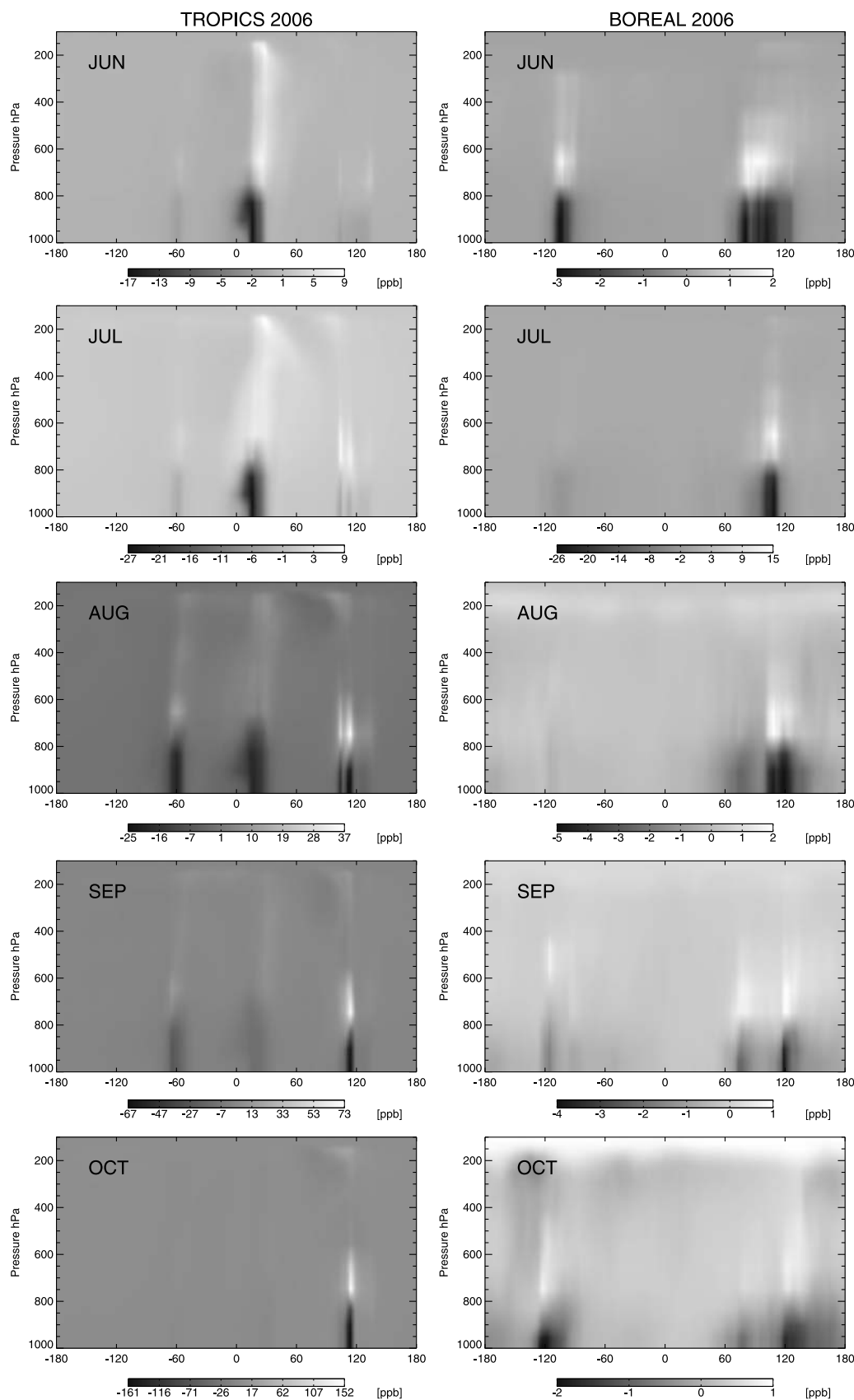


Figure 8. CO concentration differences (ppb) over tropical (0°S–30°S) and boreal (42°N–67°N) regions resulting from a GEOS-Chem model run that uses the seasonal average (JJASO 2006) injection heights inferred from TES and MLS measurements (Figure 2) minus a control model run that assumes injection only into the boundary layer.

the attenuation backscatter measurements close to our TES and MLS observations of CO.

[85] **Acknowledgments.** This work was supported by the UK Natural Environment Research Council (grant NE/E003990/1). We acknowledge discussions with the science teams of TES and MLS and with Chuntao Lui from Utah University. We also gratefully acknowledge the CALIPSO science team who routinely disseminate visualizations of their data products. We thank three anonymous reviewers who provided thorough and thoughtful comments.

References

- Andreae, M. O., et al. (2001), Transport of biomass burning smoke to the upper troposphere by deep convection in the equatorial region, *Geophys. Res. Lett.*, **28**, 951–954.
- Andreae, M. O., D. Rosenfeld, P. Artaxo, A. A. Costa, G. P. Frank, K. M. Longo, and M. A. F. Silva-Dias (2004), Smoking rain clouds over the Amazon, *Science*, **303**, 1337–1342.
- Beer, R. (2006), TES on the Aura mission: Scientific objectives, measurements, and analysis overview, *IEEE Trans. Geosci. Remote Sens.*, **44**, 1102–1105.
- Bowman, K. W., et al. (2006), Tropospheric emission spectrometer: Retrieval method and error analysis, *IEEE Trans. Geosci. Remote Sens.*, **44**, 1297–1307.
- Coheur, P.-F., et al. (2007), ACE-FTS observation of a young biomass burning plume: First reported measurements of C₂H₄, C₃H₆O, H₂CO and PAN by infrared occultation from space, *Atmos. Chem. Phys.*, **7**, 5437–5446.
- Colarco, P. R., M. R. Schoeberl, B. G. Doddridge, L. T. Marufu, O. Torres, and E. J. Welton (2004), Transport of smoke from Canadian forest fires to the surface near Washington, D.C.: Injection height, entrainment, and optical properties, *J. Geophys. Res.*, **109**, D06203, doi:10.1029/2003JD004248.
- Connor, B. J., H. Boesch, G. Toon, B. Sen, C. Miller, and D. Crisp (2008), Orbiting carbon observatory: Inverse method and prospective error analysis, *J. Geophys. Res.*, **113**, D05305, doi:10.1029/2006JD008336.
- Cook, P. A., et al. (2007), Forest fire plumes over the North Atlantic: p-TOMCAT model simulations with aircraft and satellite measurements from the ITOP/ICARTT campaign, *J. Geophys. Res.*, **112**, D10S43, doi:10.1029/2006JD007563.
- Damoah, R., et al. (2006), A case study of pyro-convection using transport model and remote sensing data, *Atmos. Chem. Phys.*, **6**, 173–185.
- Dessler, A. E., S. P. Palm, and J. D. Spinhirne (2006), Tropical cloud-top height distributions revealed by the Ice, Cloud, and Land Elevation Satellite (ICESat)/Geoscience Laser Altimeter System (GLAS), *J. Geophys. Res.*, **111**, D12215, doi:10.1029/2005JD006705.
- Duncan, B. N., J. A. Logan, I. Bey, I. A. Megretskaia, R. M. Yantosca, P. C. Novelli, N. B. Jones, and C. P. Rinsland (2007a), Global budget of CO, 1988–1997: Source estimates and validation with a global model, *J. Geophys. Res.*, **112**, D22301, doi:10.1029/2007JD008459.
- Duncan, B. N., S. E. Strahan, and Y. Yoshida (2007b), Model study of the cross-tropopause transport of biomass burning pollution, *Atmos. Chem. Phys.*, **7**, 3713–3736.
- Fiore, A., D. J. Jacob, H. Liu, R. M. Yantosca, T. D. Fairlie, and Q. Li (2003), Variability in surface ozone background over the United States: Implications for air quality policy, *J. Geophys. Res.*, **108**(D24), 4787, doi:10.1029/2003JD003855.
- Freitas, S. R., K. M. Longo, and M. O. Andreae (2006), Impact of including the plume rise of vegetation fires in numerical simulations of associated atmospheric pollutants, *Geophys. Res. Lett.*, **33**, L17808, doi:10.1029/2006GL026608.
- Fromm, M., et al. (2008), Stratospheric impact of the Chisholm pyrocumulonimbus eruption: 2. Vertical profile perspective, *J. Geophys. Res.*, **113**, D08203, doi:10.1029/2007JD009147.
- Generoso, S., I. Bey, J.-L. Attié, and F.-M. Bréon (2007), A satellite- and model-based assessment of the 2003 Russian fires: Impact on the Arctic region, *J. Geophys. Res.*, **112**, D15302, doi:10.1029/2006JD008344.
- Giglio, L. (2007), Characterization of the tropical diurnal cycle using VIRS and MODIS observations, *Remote Sens. Environ.*, **108**, 407–421.
- Herman, J. R., P. K. Bhartia, O. Torres, C. Hsu, C. Seftor, and E. Celarier (1997), Global distribution of UV-absorbing aerosols from Nimbus 7 TOMS data, *J. Geophys. Res.*, **102**, 16,911–16,922.
- Jones, D. B. A., K. W. Bowman, P. I. Palmer, J. R. Worden, D. J. Jacob, R. N. Hoffman, I. Bey, and R. M. Yantosca (2003), Potential of observations from the Tropospheric Emission Spectrometer to constrain continental sources of carbon monoxide, *J. Geophys. Res.*, **108**(D24), 4789, doi:10.1029/2003JD003702.
- Jost, H.-J., et al. (2004), In-situ observations of mid-latitude forest fire plumes deep in the stratosphere, *Geophys. Res. Lett.*, **31**, L11101, doi:10.1029/2003GL019253.
- Kahn, R. A., Y. Chen, D. L. Nelson, F.-Y. Leung, Q. Li, D. J. Diner, and J. A. Logan (2008), Wildfire smoke injection heights: Two perspectives from space, *Geophys. Res. Lett.*, **35**, L04809, doi:10.1029/2007GL032165.
- Leung, F.-Y. T., J. A. Logan, R. Park, E. Hyer, E. Kasischke, D. Streets, and L. Yurganov (2007), Impacts of enhanced biomass burning in the boreal forests in 1998 on tropospheric chemistry and the sensitivity of model results to the injection height of emissions, *J. Geophys. Res.*, **112**, D10313, doi:10.1029/2006JD008132.
- Levelt, P. F., G. H. J. van den Oord, M. R. Dobber, A. Mäkki, H. Visser, J. de Vries, P. Stammes, J. O. V. Lundell, and H. Saari (2006), The Ozone Monitoring Instrument, *IEEE Trans. Geosci. Remote Sens.*, **44**, 1093–1101.
- Livesey, N. J., M. D. Fromm, J. W. Waters, G. L. Manney, M. L. Santee, and W. G. Read (2004), Enhancements in lower stratospheric CH₃CN observed by the Upper Atmosphere Research Satellite Microwave Limb Sounder following boreal forest fires, *J. Geophys. Res.*, **109**, D06308, doi:10.1029/2003JD004055.
- Livesey, N. J., et al. (2007), EOS MLS version 2.2 level 2 data quality and description document, *Tech. Rep. D-33509*, Jet Propul. Lab., Pasadena, Calif.
- Livesey, N. J., et al. (2008), Validation of Aura Microwave Limb Sounder O₃ and CO observations in the upper troposphere and lower stratosphere, *J. Geophys. Res.*, **113**, D15S02, doi:10.1029/2007JD008805.
- Logan, J. A., I. Megretskaia, R. Nassar, L. T. Murray, L. Zhang, K. W. Bowman, H. M. Worden, and M. Luo (2008), Effects of the 2006 El Niño on tropospheric composition as revealed by data from the Tropospheric Emission Spectrometer (TES), *Geophys. Res. Lett.*, **35**, L03816, doi:10.1029/2007GL031698.
- Luderer, G., J. Trentmann, T. Winterrath, C. Textor, M. Herzog, H. F. Graf, and M. O. Andreae (2006), Modeling of biomass smoke injection into the lower stratosphere by a large forest fire (Part II): Sensitivity studies, *Atmos. Chem. Phys.*, **6**, 5261–5277.
- Mazzoni, D., J. A. Logan, D. Diner, R. Kahn, T. Lingling, and L. Qinbin (2007), A data-mining approach to associating MISR smoke plume heights with MODIS fire measurements, *Remote Sens. Environ.*, **107**, 138–148.
- Nassar, R., J. A. Logan, I. A. Megretskaia, L. T. Murray, L. Zhang, and D. B. A. Jones (2009), Analysis of tropical tropospheric ozone, carbon monoxide, and water vapor during the 2006 El Niño using TES observations and the GEOS-Chem model, *J. Geophys. Res.*, **114**, D17304, doi:10.1029/2009JD011760.
- Osterman, G., et al. (2007), EOS TES level 2 (L2) data user's guide, technical report, Jet Propul. Lab., Pasadena, Calif.
- Palmer, P. I., D. J. Jacob, D. B. A. Jones, C. L. Heald, R. M. Yantosca, J. A. Logan, G. W. Sachse, and D. G. Streets (2003), Inverting for emissions of carbon monoxide from Asia using aircraft observations over the western Pacific, *J. Geophys. Res.*, **108**(D21), 8828, doi:10.1029/2003JD003397.
- Pfister, G., P. G. Hess, L. K. Emmons, J.-F. Lamarque, C. Wiedinmyer, D. P. Edwards, G. Pétron, J. C. Gille, and G. W. Sachse (2005), Quantifying CO emissions from the 2004 Alaskan wildfires using MOPITT CO data, *Geophys. Res. Lett.*, **32**, L11809, doi:10.1029/2005GL022995.
- Prather, M. J., and D. J. Jacob (1997), A persistent imbalance in HO_x and NO_x photochemistry of the upper troposphere driven by deep tropical convection, *Geophys. Res. Lett.*, **24**, 3189–3192.
- Pumphrey, H. C., et al. (2007), Validation of middle-atmosphere carbon monoxide retrievals from the Microwave Limb Sounder on Aura, *J. Geophys. Res.*, **112**, D24S38, doi:10.1029/2007JD008723.
- Rinsland, C. P., et al. (2006), Nadir measurements of carbon monoxide distributions by the Tropospheric Emission Spectrometer onboard the Aura spacecraft: Overview of analysis approach and examples of initial results, *Geophys. Res. Lett.*, **33**, L22806, doi:10.1029/2006GL027000.
- Rodgers, C. D. (2000), *Inverse Methods for Atmospheric Sounding, Theory and Practice*, World Sci., River Edge, N. J.
- Rosenfeld, D., M. Fromm, J. Trentmann, G. Luderer, M. O. Andreae, and R. Servranckx (2007), The Chisholm firestorm: Observed microstructure, precipitation and lightning activity of a pyro-cumulonimbus, *Atmos. Chem. Phys.*, **7**, 645–659.
- Streets, D. G., Q. Zhang, L. Wang, K. He, J. Hao, Y. Wu, Y. Tang, and G. R. Carmichael (2006), Revisiting China's CO emissions after the Transport and Chemical Evolution over the Pacific (TRACE-P) mission: Synthesis of inventories, atmospheric modeling, and observations, *J. Geophys. Res.*, **111**, D14306, doi:10.1029/2006JD007118.
- Torres, O., P. K. Bhartia, J. R. Herman, Z. Ahmad, and J. Gleason (1998), Derivation of aerosol properties from satellite measurements of backscattered ultraviolet radiation: Theoretical basis, *J. Geophys. Res.*, **103**, 17,099–17,110.

- Trentmann, J., G. Luderer, T. Winterrath, M. D. Fromm, R. Servranckx, C. Textor, M. Herzog, H.-F. Graf, and M. O. Andreae (2006), Modeling of biomass smoke injection into the lower stratosphere by a large forest fire (Part I): Reference simulation, *Atmos. Chem. Phys.*, **6**, 5247–5260.
- Turquety, S., et al. (2007), Inventory of boreal fire emissions for North America in 2004: Importance of peat burning and pyroconvective injection, *J. Geophys. Res.*, **112**, D12S03, doi:10.1029/2006JD007281.
- van der Werf, G. R., J. T. Randerson, L. Giglio, G. J. Collatz, P. S. Kasibhatla, and A. F. J. Arellano (2006), Interannual variability in global biomass burning emissions from 1997 to 2006, *Atmos. Chem. Phys.*, **6**, 3423–3441.
- Vaughan, M. A., S. A. Young, D. M. Winker, K. A. Powell, A. H. Omar, Z. Liu, Y. Hu, and C. A. Hostetler (2004), Fully automated analysis of space-based lidar data: An overview of the CALIPSO retrieval algorithms and data products, *Proc. SPIE Int. Soc. Opt. Eng.*, **5575**, 16–30.
- Verma, S., et al. (2009), Ozone production in boreal fire smoke plumes using observations from the Tropospheric Emission Spectrometer and the Ozone Monitoring Instrument, *J. Geophys. Res.*, **114**, D02303, doi:10.1029/2008JD010108.
- Waters, J. W., et al. (1999), The UARS and EOS Microwave Limb Sounder (MLS) experiment, *J. Atmos. Sci.*, **56**, 194–217.
- Winker, D. M., C. A. Hostetler, M. A. Vaughan, and A. H. Omar (2006), CALIP algorithm theoretical basis document—Part 1: CALIOP instrument, and algorithms overview, *Tech. Rep. PC-SCI-202*, NASA, Washington, D. C. (Available at <http://www-calipso.larc.nasa.gov/resources/pdfs/PC-SCI-202.Part1\2-Overview.pdf>.)
- Yevich, R., and J. A. Logan (2003), An assessment of biofuel use and burning of agricultural waste in the developing world, *Global Biogeochem. Cycles*, **17**(4), 1095, doi:10.1029/2002GB001952.
- Zhang, S., J. E. Penner, and O. Torres (2005), Inverse modeling of biomass burning emissions using Total Ozone Mapping Spectrometer aerosol index for 1997, *J. Geophys. Res.*, **110**, D21306, doi:10.1029/2004JD005738.

S. Gonzi and P. I. Palmer, School of GeoSciences, University of Edinburgh, West Mains Road, Edinburgh EH9 3JN, UK. (sgonzi@staffmail.ed.ac.uk; pip@ed.ac.uk)